

Three Dimensional Near-Wall Events in an Adverse Pressure Gradient Boundary Layer

Matthew Bross

Institute of Fluid Mechanics and Aerodynamics
Universität der Bundeswehr München
Werner-Heisenberg-Weg 39,
85577 Neubiberg, Germany
matthew.bross@unibw.de

Christian J. Kähler

Institute of Fluid Mechanics and Aerodynamics
Universität der Bundeswehr München
Werner-Heisenberg-Weg 39,
85577 Neubiberg, Germany
christian.kaehler@unibw.de

Abstract

Time-resolved tomographic flow fields measured in the viscous sublayer region of a turbulent boundary layer subjected to an adverse pressure gradient (APG) are examined with the aim to resolve and characterize reverse flow events at $Re_\tau = 5000$ and $10\,000$. The fields were measured using a novel high resolution tomographic particle tracking technique. It is shown that this technique is able to fully resolve mean and time dependent features of the complex three-dimensional flow with high accuracy down to very near-wall distances ($\sim 10\ \mu\text{m}$). From time resolved Lagrangian particle trajectories, statistical information as well as instantaneous topological features of near-wall flow events are deduced. Similar to the zero pressure gradient case (ZPG), it was found that individual events with reverse flow components still occur relatively rarely under the action of the pressure gradient investigated here. However, reverse flow events are shown to appear in relatively organized groupings in both spanwise and streamwise directions. Moreover, it was observed that some of the reverse flow events are associated with streamwise vortices that convect along with low-speed streaks. This can be explained by the tilted nature of these vortices with respect to the main flow direction. The reverse flow events associated with tilted streamwise vortices inside low-speed streaks have been observed to spatially extend over 100 viscous units. As different mechanisms can lead to reverse flow events, these events are not universal. However, the results and discussion make it possible to understand the appearance of reverse flow events based on the interaction of well known coherent flow structures.

Introduction

The behavior of turbulent boundary layers is directly related to the aerodynamic performance of many technical devices. For this reason the physical understanding of these types of flows is of great scientific and technological interest and importance. While the turbulent flows along a flat plate with zero pressure gradients were investigated in great detail in the last decades, as seen in the extensive review by (Wallace, 2012), the effect of a pressure gradient is by far less understood see Knopp *et al.* (2015) and references therein. Moreover, the details of the transition from the fully attached to the partly and fully separated flow states is widely unknown (Michael & Rainer, 2002; Skåre & Krogstad, 1994).

Of particular interest for the present investigation are relatively rare instances of small localized reverse flow events because they might be the nucleus for the generation of macroscopic flow separation in adverse pressure gradient boundary layers. In recent years, the numerical prediction of reverse flow events in channel (Lenaers *et al.*, 2012) and turbulent boundary layer flows (Spalart & Coleman, 1997) has achieved strong attention. As the spatial extent of these events is very small according to Cardesa *et al.* (2014), and their occurrence extremely seldom (Schlatter & Örlü, 2010), their detection in experiments was quite challenging. However, in recent

years their existence could be confirmed experimentally using long-range micro PIV (Willert, 2015) and micro pillars (Brücker, 2015) techniques.

The aforementioned numerical and experimental studies were performed mostly at relatively low Reynolds numbers ($Re_\tau < 2000$) and for zero pressure gradients. The probability of such events occurring was measured to be around 0.01% (Willert, 2015), which makes statistical analysis of reverse flow events difficult. Furthermore, the experimental investigations only yield information about the footprint of the reverse flow events on the wall shear stress (Brücker, 2015) and the characteristics of the structures in an arbitrary slice selected by the light-sheet used for the planar PIV and PTV investigation by Kähler (2014) and Willert (2015).

The motivation for measuring in the near-wall region is to investigate the relationship between rare near-wall flow effects with coherent large scale motion in the near-wall and logarithmic region of the turbulent boundary layer. This connection would allow for the manipulation of these reverse flow events by means of macroscopic flow control methods. This may be beneficial for delaying flow separation (by reducing the number of reverse flow events) or by decreasing the viscous drag of fully attached flows (by increasing the appearance of reverse flow events). It is possible that the reverse flow events are associated with the motion of near-wall low-speed streaks (Kline *et al.*, 1967; Smith & Metzler, 1983) or even low-momentum superstructures (Buchmann *et al.*, 2016) but, this has not been demonstrated experimentally or numerically so far. In contrast to the reverse flow events, the low-speed streaks frequently appear at near-wall locations. Therefore, it is likely that a specific interaction between near-wall low-speed streaks and large-scale low-momentum superstructures is necessary to slow down the flow sufficiently at the wall so that rare reverse near-wall flow can develop.

In the investigation presented herein, the topology and statistics of near-wall reverse events will be discussed and their connection with the aforementioned large scale coherent structures is outlined. As these reverse flow events appear very seldom in low Reynolds number turbulent boundary layers along flat plates with zero pressure gradient we examine these structures and under the effect of an adverse pressure gradient to make a statistical analysis of the rare reverse flow events possible. Furthermore, it can be examined if the rare reverse flow events are universal or if multiple events exist with different topology. It will also be possible to examine their scale and dynamics and if the events appear randomly in space and time or in packets with a characteristic frequency. In contrast to other investigation we also study these events at larger Reynolds numbers to validate if the reverse flow events are a low Reynolds number phenomena. To resolve the spatial and temporal details of the near-wall flow with high accuracy and spatial resolution, a novel tomographic tracking technique was developed to record time-resolved flow fields in the viscous sublayer. Furthermore, information about

the flow in the spanwise direction is now available from the results present herein, which is absent from previous two-dimensional PIV studies.

Experimental Systems

Turbulent boundary layer experiments were performed at the Universität der Bundeswehr München in the Atmospheric Wind tunnel Munich (AWM). The Eiffel type wind tunnel has a 22 m long test section with a cross section of $2 \times 1.8 \text{ m}^2$ and flow velocities up to 40 m/s can be achieved. A 7 m long polished aluminum boundary layer model consisting of two S-shaped deflections on either end of a 4 m flat plate zero pressure gradient (ZPG) section, was installed along the side wall of the wind tunnel. The adverse pressure gradient (APG) region (downstream of the ZPG part) was fitted with a glass viewing window of size $0.26 \times 0.59 \text{ m}^2$, see figure 1. The X-direction indicates the streamwise distance along the wind tunnel, starting at the beginning of the model. Qualification measurements for the boundary layer along this model are detailed in (Reuther *et al.*, 2015).

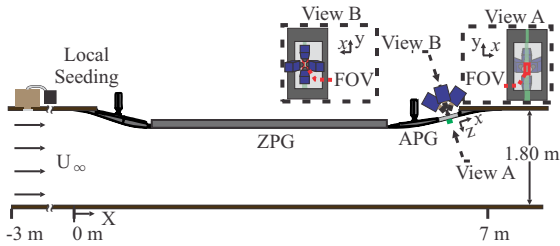


Figure 1: Plan view of boundary layer model in AWM and tomographic PTV setup.

The tracer particles, $1 \mu\text{m}$ DEHS particles introduced locally, in the APG region were illuminated in a wall parallel plane by a continuous wave laser (Kvant Laser) with maximum output power of 8 W and $532 \mu\text{m}$ wavelength. The laser beam was formed into a uniform sheet of 40 mm width and thickness of 1 mm and aligned directly adjacent to the wall.

High-speed particle image sequences for the tomographic PTV measurement were captured by 4 high-speed CMOS cameras with 36GB of RAM (Dimax-S4, PCO GmbH) mounted in 30° cross configuration behind the glass viewing window in the APG, see figure 1. The coordinate system (x, y, z) defined in View A corresponds to the wall-parallel direction in the APG, spanwise direction, and wall-normal direction respectively. Using 50 mm/f2.8 Zeiss objectives and Scheimpflug mounts, the resulting resolution in the center of the FOV was $\sim 25 \mu\text{m}/\text{pix}$. However, the resolution of the measurement is much better as the particle images can be located with sub-pixel resolution (Kähler *et al.*, 2012a,b; Cierpka *et al.*, 2013a,b). By dividing the pixel pitch of the HS camera ($11 \mu\text{m}/\text{pix}$) the resulting magnification in the center of the FOV was $M = 25 \text{ (px/mm)}$, resulting in a field of view of (x, y, z) and $17 \times 25 \times 0.8 \text{ mm}^3$ and $15 \times 23 \times 0.8 \text{ mm}^3$ for $\text{Re}_\tau = 5000$ and $\text{Re}_\tau = 10\,000$ data sets, respectively. The boundary layer thickness, determined from previous large field measurements at the measurement location, was $\delta_{99} \approx 200 \text{ mm}$.

The evaluation of the data was performed with in-house tomographic reconstruction (Fuchs *et al.*, 2016) and time resolved particle tracking (based on Cierpka *et al.* (2013a)) algorithms. In contrast to PIV, particle tracking algorithms greatly enhance the spa-

tial resolution as spatial averaging over an interrogation window is avoided (Kähler *et al.*, 2012a,b). However, reliable particle identification can be difficult for high seeding concentrations especially when the mean particle distance is much smaller than the mean displacements. Since modern high-speed cameras allow for the time-resolved sampling of the flow, the temporal information can be used to enhance the tracking procedure (Cierpka *et al.*, 2013a; Kähler *et al.*, 2016; Schanz *et al.*, 2016). This method is especially suited for the correct estimation of the velocity and vector position for trajectories with strong curvature (Cierpka *et al.*, 2013a; Scharnowski & Kähler, 2012) as typically for the reverse flow events in the near-wall region of turbulent boundary layers (Bross & Kähler, 2016; Schröder *et al.*, 2016).

Mean Field

For the proper normalization of the flow data the friction velocity has to be estimated from the slope of the mean velocity profile at the wall. The mean velocity profile was computed (from 40 000 image sequences) by sorting the trajectories into equally spaced bins in the z -direction and extending over the xy -planes. For the mean flow results, bins of z -direction spacing $12.5 \mu\text{m}$ and $20 \mu\text{m}$ for $\text{Re}_\tau = 5000$ and $10\,000$, respectively, were used. These bin spacings were selected so that sufficient data points appear within each bin. Moreover, any remaining outliers were eliminated with proper continuous fitting of the velocity distribution in each bin.

In the very near-wall region naturally there will be a lower concentration of seeding particles. The low seeding concentration may have a strong effect on the statistical quantities because outliers in this region, with large displacement values, significantly alter the mean value in these bins. To account for this, a continuous distribution of each bin was fit to the points with by means of a Gauss function. With this fit applied, the mean field in each bin can be calculated by either taking the peak of the Gauss curve or only considering values within 2σ . For this investigation velocities within 2σ of the fit applied to each bin were used to created the mean field shown in figure 2.

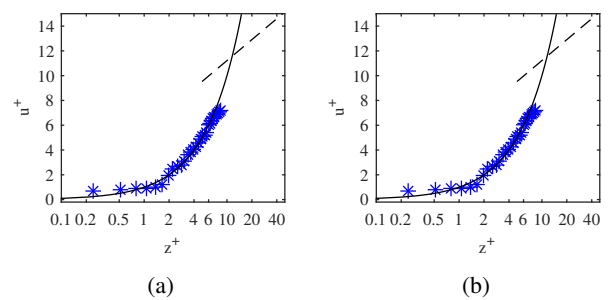


Figure 2: Mean field in viscous scaling for (a) $\text{Re}_\tau = 5000$ (b) and $10\,000$.

For this data set it appears that correct mean values were achieved for between $0.25 < z^+ < 9$ and $0.2 < z^+ < 12$ for $\text{Re}_\tau = 5000$ and $10\,000$ respectively. Due to having reliable data points in the linear region ($z^+ = u^+$) of the turbulent boundary layer flow, calculating the viscous scaling is straight forward. A linear fit of \bar{u} vs. \bar{z} , where $u = \bar{u} + u'$ and \bar{z} is the average bin position in the z -direction, allows for the calculation of $u_\tau = \sqrt{v d\bar{u}/d\bar{z}}|_{z=0}$ and the z -intercept indicates the wall location. Therefore, $u^+ = \bar{u}/u_\tau$ and $z^+ = z u_\tau / \nu$ can directly be calculated. Our results show that for $\text{Re}_\tau = 5000$ and $10\,000$, $u_\tau = 0.201$ and $u_\tau = 0.370$. This corresponds to viscous units of $\nu/u_\tau = 78 \mu\text{m}$ and $\nu/u_\tau = 43 \mu\text{m}$.

Statistics of Reverse Flow Events

It is suspected that the near-wall reverse flow events remain relatively close to the wall and do not extend past the viscous sublayer because of the rapidly increasing flow velocity with growing wall distance. This means that the probability of detecting these events will decrease with increasing wall distance until these events will be no longer observable. Consequently, the probability in finding these events is the largest at very small wall distances. However, due to the drop of the seeding concentration towards the wall, the likelihood of detecting these events in real measurements also decreases towards the wall and therefore a maximum must exist at a certain wall distance where the detectability is the largest. For a statistical analysis of these events, it is important to know this maximum in order to minimize bias effects in detecting the number of events.

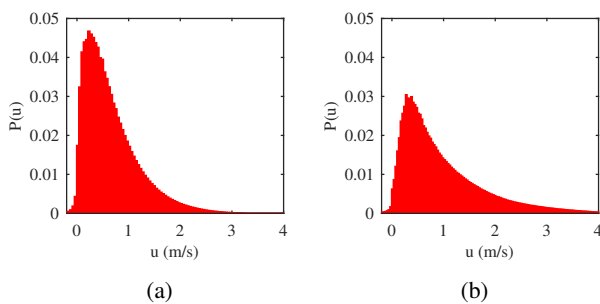


Figure 3: Streamwise displacements for $0 < z^+ < 6$ range (a) $Re_\tau = 5000$, probability of reverse event 1% and (b) $Re_\tau = 10\,000$, probability of reverse event 0.5%.

The first step for identifying reverse flow events is to detect the all reverse flow vectors. However, since reverse flow events most likely comprise of many negative velocities, it is important to first filter out vectors that are less likely to be associated with reverse events and secondly determine the location in the wall-normal direction where they occur. The first filtering step involves removing reverse flow trajectories that have a length of only one. Some of these one length trajectories may be valid, i.e. particle images located at the edges of the event, but since it is expected that reverse events occur close to the wall and at slow velocities, it is expected that only the longer trajectories yield relevant physical information about the events. Therefore, for further analysis only negative streamwise vectors in trajectories of length > 1 are considered to be physically significant. A PDF of reverse event vectors distributed in the wall normal direction indicates that more than 85% of these events occur at $z^+ < 5$ for $Re_\tau = 5000$ and 60% for $Re_\tau = 10\,000$. These distribution show nicely that the maximum number of events can be detected at $z^+ \approx 1$ and 2 respectively.

Now that the statistically important reverse vectors have been identified and their location in the wall normal direction has been quantified, the probability of these vectors appearing with respect to all displacements for $0 < z^+ < 6$ can be seen in figure 3. Even for this range of z^+ , the probability of a reverse flow vector occurring is relatively low, 0.01 or 1% and 0.005 or 0.5% for $Re_\tau = 5000$ and 10 000 respectively. This value represents a much larger value than presented in other measurements for ZPG boundary layer flow. However, it must be kept in mind that a reverse event is comprised of many reverse particle tracks and therefore the occurrence probability of reverse flow is much smaller, as will be discussed in the following section.

Reverse Flow Event Detection in a Time Series

In the preceding sections, efforts to qualify the experimental data and assess statistical properties of individual velocity vectors have been made. However, there must be a distinction between an individual reverse vector and a reverse event. The distinction is made more evident by visualizing how these reverse vectors are grouped throughout a time series. Therefore, in figure 4 negative velocity vectors are grouped into bins of 50 images for selected time sequence taken from the $Re_\tau = 5000$ data set. Bins are filtered by removing bins that only have one unique trajectory inside and if that trajectory consists of less than three points. This means that reverse flow events which are only sampled by one single particle image pair or only appear along the outer edge of the events, are not considered for the analysis as both cases yield very little information about the topology and dynamics of the events. First, it should be noted that many intervals exist where no reverse flow events are detected and the length of the intervals can be quite large, as expected from previous investigations. Second, it appears that reverse flow events appear in groups. This does not necessarily mean that they interact in these groups, but once a reverse flow event appears it is likely to see more events within a short time period. Third, from the amplitude and distribution of the signal in this plot it is evident that there are several different classes or types of reverse events in terms of their lifetime and spatial size. By using analysis of this type, it is possible to locate image ranges where significant reverse flow is occurring. Furthermore, if one roughly considers the probability of major reverse events (bins with amplitudes larger than 2000) it is one order of magnitude less than previously calculated for individual reverse vectors, i.e. 0.1% compared to 1%.

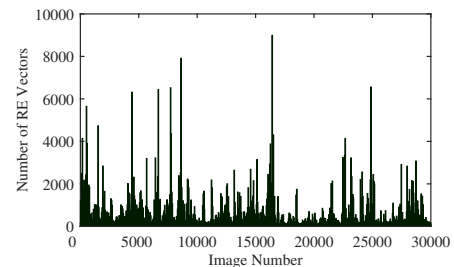


Figure 4: Reverse event detection $Re_\tau = 5000$.

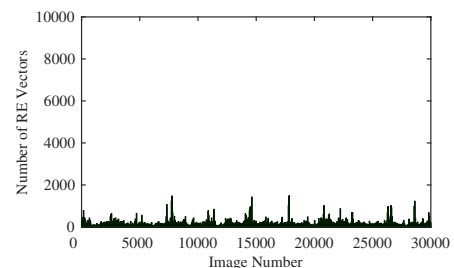


Figure 5: Reverse event detection $Re_\tau = 10\,000$.

A similar analysis was performed in figure 5 for a selected

time series from the $Re_\tau = 10\,000$ data set. The first observation made from this figure is that the amplitude of reverse events in time sequence bins is much less than seen in figure 4. If the events are roughly counted by grouping of more than 1000 vectors, the probability of a reverse event occurring is also an order of magnitude less than previously calculated for individual reverse vectors, i.e. 0.05% compared to 0.5%. This shows that the Reynolds number appears to have a significant effect on the reverse flow events and it is possible that these events vanish at very large Reynolds numbers.

To examine if there is a connection between reverse events and strong spanwise motion. The flow direction angle was calculated using just the streamwise and spanwise vector components (the wall-normal velocity component is of little effect when compared to the other components). The probability of a given flow direction in polar coordinates is provided in the figure 6 for both data sets. In this plot 0° indicates flow in the positive x-direction and -180° is flow purely in the negative x-direction. What is immediately evident from these plots is that flow has a much larger probability (2 orders of magnitude) of being in the streamwise direction rather than the flow with a component in the negative streamwise direction ($\pm 90^\circ$).

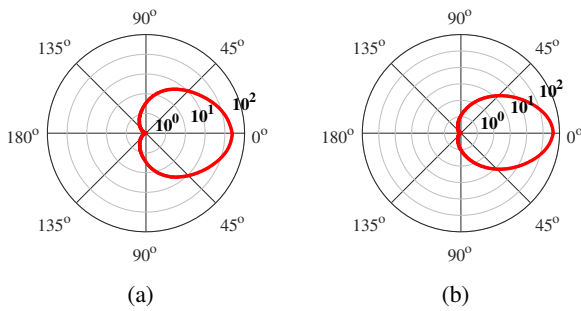


Figure 6: Relative flow direction probability in polar coordinates for $Re_\tau = 10\,000$.

Secondly, it is evident that the relative probability of a reverse vector occurring is orders of magnitude less than purely streamwise events for both figures 6(a) and 6(b). Second, as shown before in section , the reverse vectors are less probable for $Re_\tau = 10\,000$ than for $Re_\tau = 5000$. Which suggests that reverse flow might be a low Reynolds number effect and for Reynolds larger than measured herein the decrease in probability continues. Third, these plots show is that reverse events with a flow direction of $\pm 70^\circ$ are more probable by one order of magnitude than events purely in the reverse direction. This implies that a coherent structure producing a significant spanwise motion seems to be essential for the generation of reverse flow events.

Reverse Flow Event Visualization

In order to access the topology of the flow structure during these rare reverse events, a selection of reverse events from the $Re_\tau = 5000$ data set are visualized by plotting three-dimensional trajectories colored with the streamwise velocity. The events in the forgoing section were selected by choosing several events that had many reverse flow vectors over a short images range according to figure 4. The first case is provided in figure 7a where trajectories are plotted over a time series of 100 images. In the right image (plot in x and y directions), it is immediately obvious the streaky structure of low and high-momentum flow. In the low-momentum regions,

reverse flow events appear most prominently. These events appear as a group across the entire streamwise extent of the measurement volume or approximately 150 viscous units. It is evident that the regions of reverse flow are associated with a low-speed streak but also the small reverse flow events are at locations where low-speed streaks are present. Thus it can be concluded that low-speed streaks are a necessary condition for the existence of reverse flow events in turbulent boundary layers. Furthermore, it can be seen that the extent of the the events in the wall normal direction is limited to around $z^+ = 5$.

To demonstrate that nature of these reverse events is not universal, another instance of reverse is plotted in figure 7b. In this particular case trajectories are plotted over a time series of 50 images. In contrast to figure 7a the flow is dominated by one large spanwise (y-direction) directed event. Trajectories appear grouped in a defined spatial location and extend over an area of 10 mm by 10 mm in the streamwise and spanwise directions. Remarkable is the significant spanwise motion of this event which was not observed to this extent in figure 7a. It seems plausible that the large spanwise motion must be associated with longitudinal vortices. This is confirmed by the cross-plane visualization. If the axis of a streamwise vortex is slightly tilted with respect to the mean flow direction, these longitudinal vortices can generate reverse flow events, provided the vortex travels with a sufficiently low convection velocity, which is possible when the vortex is embedded inside a low-speed streak and a low-momentum superstructure is located above the low-speed streak. Consequently this generation mechanism is based on a triple interaction between low-momentum superstructures, low-speed streaks and tilted streamwise vortices. If the local convection velocity is increased locally by high-momentum near-wall streaks or globally by high-momentum superstructures, reverse flow events are suppressed and cannot appear. This demonstrates a connection between the superstructures in the logarithmic part of the boundary layer and the near-wall flow structures.

Concluding Remarks

The work presented herein, investigated the rare reverse flow events in an APG turbulent boundary layer flow at $Re_\tau = 5000$ and $10\,000$ by using a novel time-resolved tomographic PTV technique developed at the institute. The results show that these events appear mostly in the near-wall region below $z^+ < 5$ for both Reynolds numbers investigated. The physical characteristics of reverse events were discussed by observing trajectory plots over several representative image sequences. From these images it follows that there exist several different forms of these events in terms the spatial extent and intensity of negative velocity. It was shown that the large events extend in both spanwise and streamwise directions on the millimeter scale, which is larger than the dimensions given in the literature for the ZPG case at low Reynolds numbers. Furthermore, it was observed that the reverse flow events are much less probable for the larger of the two Reynolds numbers measured in this experiment. It is possible that at even higher Reynolds numbers, reverse flow events like these do not occur any more.

In all cases of reverse flow events displayed, a region of low-momentum was observed in the area in and around the reverse events which was associated with the well known near-wall low-speed streaks. Therefore, it can be concluded that low-speed streaks are a necessary condition for the appearance of reverse flow events. But the low detectability of the reverse flow events indicates that another phenomenon must take place simultaneously to generate the conditions which may lead to these rare events. The results indicate that a low-momentum superstructure must be superimposed on the low-speed streak which has a sufficiently low-momentum that creates the conditions for the generation of a reverse flow event.

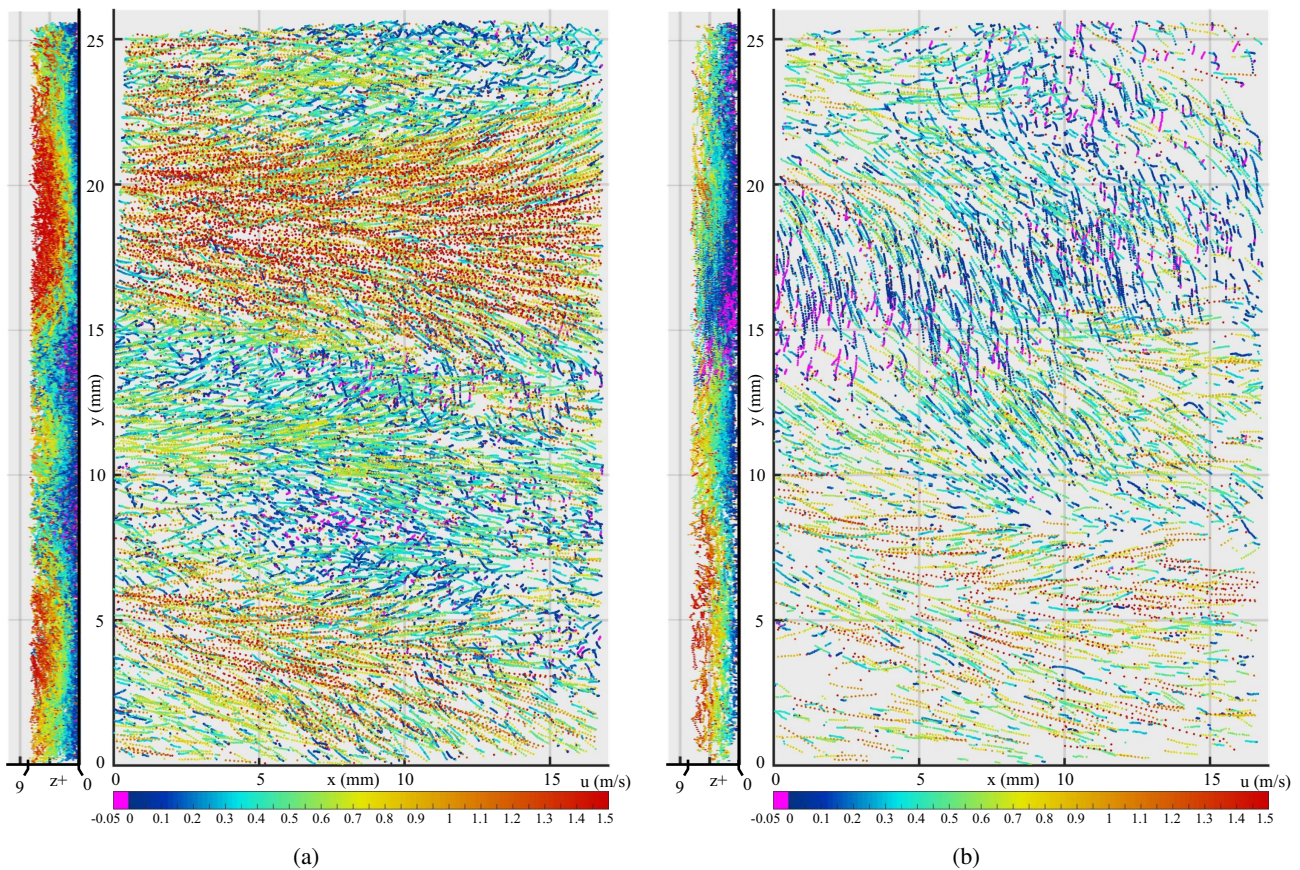


Figure 7: Three-dimensional trajectories during reverse flow event at $Re_{\tau} = 5000$. Trajectories are colored with streamwise velocity, u (m/s), where positive flow is from left to right.

Consequently, when high-momentum superstructures are superimposed on the near-wall low-speed streaks, the convection velocity increases and reverse flow events are not able to appear. Due to the length of the high-momentum superstructures (on average streamwise length of $15\delta - 20\delta$, Hutchins & Marusic (2007a,b)) long intervals exist where no reverse flow events can be observed. However, if a low-momentum superstructure is present that produces sufficient velocity deficit near the wall (Buchmann *et al.*, 2016), single or groups of reverse flow events can be observed if near-wall streaks of sufficient low momentum exist.

Furthermore, evidence of small longitudinally oriented vortices is demonstrated by the large spanwise directed trajectories in the vicinity of reverse events. The probability of reverse flow vectors having a significant spanwise component was shown to be an order of magnitude larger than purely reverse events for both Reynolds numbers measured. Regions of strong spanwise flow that are associated with reverse flow are correlated with regions of low-momentum again indicates that longitudinal vortices that reside within the near-wall low-speed streaks are able to generate reverse flow events. However, these kind of reverse flow events only occur when the axis of the streamwise vortices is slightly tilted with respect to the mean flow direction, generating flow in both the spanwise and upstream (reverse) directions. As this only creates a reverse flow event if the convection velocity of the streamwise vortex is sufficiently low, these events could be only observed when the longitudinal vortex was embedded in a near-wall low-speed streak and has sufficiently low velocity caused by the superposition of a low-momentum superstructure on the low-speed near-wall streak. This triple interaction is unlikely as well, making the observation of

reverse flow events very seldom, which was seen in this investigation.

The results clearly show that reverse flow events are not universal due to the different generation mechanisms and it is evident that their generation requires a direct interaction of near-wall low-speed streaks and low-momentum superstructures. Due to the large level of the velocity deficit required by superimposing both low-momentum structures, the total number of events will be low as observed herein. However, whenever the specific conditions are reached, multiple reverse flow events can be generated one after another. This explains why these events appear on different time scales.

This work is supported by the Priority Programme SPP 1881 Turbulent Superstructures the Deutsche Forschungsgemeinschaft.

REFERENCES

- Bross, M. & Kähler, C.J. 2016 Time-Resolved 3D-PTV Analysis of Near Wall Reverse Flow Events in APG Turbulent Boundary Layers. In *18th Inter. Symp. on the App. of Laser and Imaging Tech. to Fluid Mech.*, July 4-7, Lisbon, Portugal.
- Brücker, Ch. 2015 Evidence of rare backflow and skin-friction critical points in near-wall turbulence using micropillar imaging. *Phys. of Fluids* **27** (3), 1–7.
- Buchmann, N.A., Küçükosman, Y.C., Ehrenfried, K. & Kähler, C.J. 2016 Wall pressure signature in compressible turbulent boundary layers. In *Progress in Wall Turbulence 2*, pp. 93–102. Springer International Publishing.
- Cardesa, J.I., Monty, J., Soria, J. & Chong, M. 2014 Skin-friction

- critical points in wall-bounded flows. *Journal of Physics: Conference Series* **506**.
- Cierpka, C., Lütke, B. & Kähler, C.J. 2013a Higher order multi-frame particle tracking velocimetry. *Exp. Fluids* **54**, 1533.
- Cierpka, C., Scharnowski, S. & Kähler, C.J. 2013b Parallax correction for precise near-wall flow investigations using particle imaging. *Appl. Opt.* **52** (12), 2923–2931.
- Fuchs, T., Hain, R & Kähler, C.J. 2016 Double-frame 3D-PTV using a tomographic predictor. *Exp. Fluids* **57** (11), 174.
- Hutchins, N. & Marusic, I. 2007a Evidence of very long meandering features in the logarithmic region of turbulent boundary layers. *J. Fluid Mech.* **579**, 1–29.
- Hutchins, N. & Marusic, I. 2007b Large-scale influences in near-wall turbulence. *Phil. Trans. R. Soc. A* **365**, 647–664.
- Kähler, C.J. 2014 Large-Scale Structures in Turbulent Boundary Layers. In *ETMM10: 10th Int. ERCOFTAC Symp. on Eng. Turbulence Modelling and Meas., Sept 17-19, Marbella, Spain*.
- Kähler, C.J., Astarita, T., Vlachos, P., Sakakibara, J., Hain, R., Discetti, S., La Foy, R. & Cierpka, C. 2016 Main results of the 4th international PIV challenge. *Exp. Fluids* **57**, 97.
- Kähler, C.J., Scharnowski, S. & Cierpka, C. 2012a On the resolution limit of digital particle image velocimetry. *Exp. Fluids* **52**, 1629.
- Kähler, C.J., Scharnowski, S. & Cierpka, C. 2012b On the uncertainty of digital PIV and PTV near walls. *Exp. Fluids* **52**, 1641.
- Kline, S.J., Reynolds, W.C., Schraub, F.A. & Runstadler, P.W. 1967 The structure of turbulent boundary layers. *J. Fluid Mech.* **30**, 741–773.
- Knopp, T., Buchmann, N.A., Schanz, D., Eisfeld, B., Cierpka, C., Hain, R., Schröder, A. & Kähler, C.J. 2015 Investigation of scaling laws in a turbulent boundary layer flow with adverse pressure gradient using PIV. *Journal of Turbulence* **16** (3), 250–272.
- Lenaers, P., Li, Qiang, Brethouwer, G., Schlatter, P. & Örlü, R. 2012 Rare backflow and extreme wall-normal velocity fluctuations in near-wall turbulence. *Phys. of Fluids* **24** (3), 1–17.
- Michael, M. & Rainer, F. 2002 DNS of a turbulent boundary layer with separation. *Inter. J. of Heat and Fluid Flow* **23** (5), 572 – 581.
- Reuther, N., Scharnowski, S. & Hain, R. 2015 Experimental investigation of adverse pressure gradient turbulent boundary layers by means of large-scale PIV. In *11th Inter. Symp. on Particle Image Velocimetry, September 14-16, Santa Barbara, USA*.
- Schanz, D., Gesemann, S. & Schröder, A. 2016 Shake-The-Box: Lagrangian particle tracking at high particle image densities. *Exp. Fluids* **57**, 70.
- Scharnowski, S. & Kähler, C.J. 2012 On the effect of curved streamlines on the accuracy of PIV vector fields. *Exp. Fluids* **54** (1), 1435.
- Schlatter, P. & Örlü, R. 2010 Assessment of direct numerical simulation data of turbulent boundary layers. *J. Fluid Mech.* **659**, 116–126.
- Schröder, A., Schanz, D., Geisler, R. & Gesemann, S. 2016 Investigations of coherent structures in near-wall turbulence and large wall-shear stress events using Shake-The-Box. In *18th Inter. Symp. on the App. of Laser and Imaging Tech. to F. Mech., July 4-7, Lisbon, Portugal*.
- Skåre, P. & Krogstad, P. 1994 A turbulent equilibrium boundary layer near separation. *J. Fluid Mech.* **272**, 319–348.
- Smith, C.R. & Metzler, S.P. 1983 The characteristics of low-speed streaks in the near-wall region of a turbulent boundary layer. *J. Fluid Mech.* **129**, 27–54.
- Spalart, P.R. & Coleman, G.N. 1997 Numerical study of separation bubble with heat transfer. *Eurp. J. Mech. B - Fluids* **16**, 169–187.
- Wallace, J.M. 2012 Highlights from 50 years of turbulent boundary layer research. *J. Turbulence* **13**, 1–70.
- Wereley, S.T. & Meinhart, C.D. 2001 Second-order accurate particle image velocimetry. *Exp Fluids* **31**, 258–268.
- Willert, C.E. 2015 High-speed particle image velocimetry for the efficient measurement of turbulence statistics. *Exp. Fluids* **56**, 17.